

# Memristors with diffusive dynamics as synaptic emulators for neuromorphic computing

Zhongrui Wang<sup>1†</sup>, Saumil Joshi<sup>1†</sup>, Sergey E. Savel'ev<sup>2</sup>, Hao Jiang<sup>1</sup>, Rivu Midya<sup>1</sup>, Peng Lin<sup>1</sup>, Miao Hu<sup>3</sup>, Ning Ge<sup>3</sup>, John Paul Strachan<sup>3</sup>, Zhiyong Li<sup>3</sup>, Qing Wu<sup>4</sup>, Mark Barnell<sup>4</sup>, Geng-Lin Li<sup>5</sup>, Huolin L. Xin<sup>6</sup>, R. Stanley Williams<sup>3</sup>, Qiangfei Xia<sup>1</sup> and J. Joshua Yang<sup>1\*</sup>

**The accumulation and extrusion of  $\text{Ca}^{2+}$  in the pre- and postsynaptic compartments play a critical role in initiating plastic changes in biological synapses. To emulate this fundamental process in electronic devices, we developed diffusive Ag-in-oxide memristors with a temporal response during and after stimulation similar to that of the synaptic  $\text{Ca}^{2+}$  dynamics. *In situ* high-resolution transmission electron microscopy and nanoparticle dynamics simulations both demonstrate that Ag atoms disperse under electrical bias and regroup spontaneously under zero bias because of interfacial energy minimization, closely resembling synaptic influx and extrusion of  $\text{Ca}^{2+}$ , respectively. The diffusive memristor and its dynamics enable a direct emulation of both short- and long-term plasticity of biological synapses, representing an advance in hardware implementation of neuromorphic functionalities.**

Complementary metal–oxide–semiconductor circuits have been employed to mimic synaptic  $\text{Ca}^{2+}$  dynamics, but three-terminal devices bear limited resemblance to bio-counterparts at the mechanism level and require significant numbers and complex circuits to simulate synaptic behaviour<sup>1–3</sup>. A substantial reduction in footprint, complexity and energy consumption can be achieved by building a two-terminal circuit element, such as a memristor directly incorporating  $\text{Ca}^{2+}$ -like dynamics. Various types of memristor based on ionic drift (drift-type memristor)<sup>4–8</sup> have recently been utilized for this purpose in neuromorphic architectures<sup>9–15</sup>. Although qualitative synaptic functionality has been demonstrated, the fast switching and non-volatility of drift memristors optimized for memory applications do not faithfully replicate the nature of plasticity. Similar issues also exist in metal–oxide–semiconductor-based memristor emulators<sup>16–18</sup>, although they are capable of simulating a variety of synaptic functions including spike-timing-dependent plasticity (STDP). Recently, researchers adopted second-order drift memristors to approximate the  $\text{Ca}^{2+}$  dynamics of chemical synapses by utilizing thermal dissipation<sup>19</sup> or mobility decay<sup>20</sup>, which successfully demonstrated STDP with non-overlapping spikes and other synaptic functions, representing a significant step towards bio-realistic synaptic devices. This approach features repeatability and simplicity, but the significant differences of the physical processes from actual synapses limit the fidelity and variety of desired synaptic functions. A device with similar physical behaviour to the biological  $\text{Ca}^{2+}$  dynamics would enable improved emulation of synaptic function and broad applications to neuromorphic computing. Here we report such an emulator, which is a memristor based on metal atom diffusion and spontaneous nanoparticle formation, as determined by *in situ* high-resolution transmission electron microscopy (HRTEM) and nanoparticle dynamics simulations. The dynamical properties of the diffusive memristors were confirmed to be functionally equivalent to  $\text{Ca}^{2+}$  in bio-synapses, and their operating

characteristics were experimentally verified by demonstrating both short- and long-term plasticity, including synaptic functions that have not been unambiguously demonstrated previously.

The diffusive memristor illustrated in Fig. 1a consists of two Pt or Au inert electrodes sandwiching a switching layer of a dielectric film with embedded Ag nanoclusters (Methods). X-ray photoelectron spectroscopy revealed that the Ag was metallic, which was further confirmed by HRTEM micrographs showing Ag nanocrystals in  $\text{SiO}_x\text{N}_y\text{:Ag}$  (Supplementary Figs 1 and 2). These devices are similar to electrochemical metallization memory<sup>21–26</sup> cells in terms of utilizing mobile species of noble metals, but they differ substantially in terms of the structural and electrical biasing symmetry, metal concentration and profile, and transient switching behaviour. An applied voltage above an apparent threshold abruptly switched the device to a conductance state limited by an external compliance current (Fig. 1b). To demonstrate that the device spontaneously relaxed back to an insulating configuration on removing the bias (without applying an opposite polarity voltage), repeatable *I–V* loops with only positive applied voltages were used in collecting the data in Fig. 1b. Symmetric hysteresis loops were observed with the opposite polarity bias (Supplementary Fig. 3), showing that the threshold switching is unipolar in nature and significantly different from non-volatile drift-type memristors, especially in the OFF-switching process. The micro-devices represented by Fig. 1a have an area of  $10\text{ }\mu\text{m} \times 10\text{ }\mu\text{m}$  and nano-devices with an area of  $100\text{ nm} \times 100\text{ nm}$  exhibited similar switching behaviours (Supplementary Fig. 4). The resistance ratio between the conducting and insulating states was five orders of magnitude in  $\text{SiO}_x\text{N}_y\text{:Ag}$  and over ten orders in  $\text{HfO}_x\text{:Ag}$  devices, the highest reported in threshold switching devices so far<sup>27–30</sup>. The volatile switching had sharp turn-on slopes of  $\sim 10\text{ mV decade}^{-1}$  in  $\text{MgO}_x\text{:Ag}$  and  $\text{SiO}_x\text{N}_y\text{:Ag}$ , and an extraordinary  $\sim 1\text{ mV decade}^{-1}$  in  $\text{HfO}_x\text{:Ag}$ , the sharpest demonstrated to date<sup>27–30</sup>. The high current capability and large resistance ratio enable diffusive memristors to be utilized as

<sup>1</sup>Department of Electrical and Computer Engineering, University of Massachusetts, Amherst, Massachusetts 01003, USA. <sup>2</sup>Department of Physics, Loughborough University, Loughborough LE11 3TU, UK. <sup>3</sup>Hewlett Packard Labs, Palo Alto, California 94304, USA. <sup>4</sup>Air Force Research Lab, Information Directorate, Rome, New York 13441, USA. <sup>5</sup>Biology Department, University of Massachusetts, Amherst, Massachusetts 01003, USA. <sup>6</sup>Center for Functional Nanomaterials, Brookhaven National Laboratory, Upton, New York 11973, USA. <sup>†</sup>These authors contributed equally to this work. \*e-mail: [jjyang@umass.edu](mailto:jjyang@umass.edu)

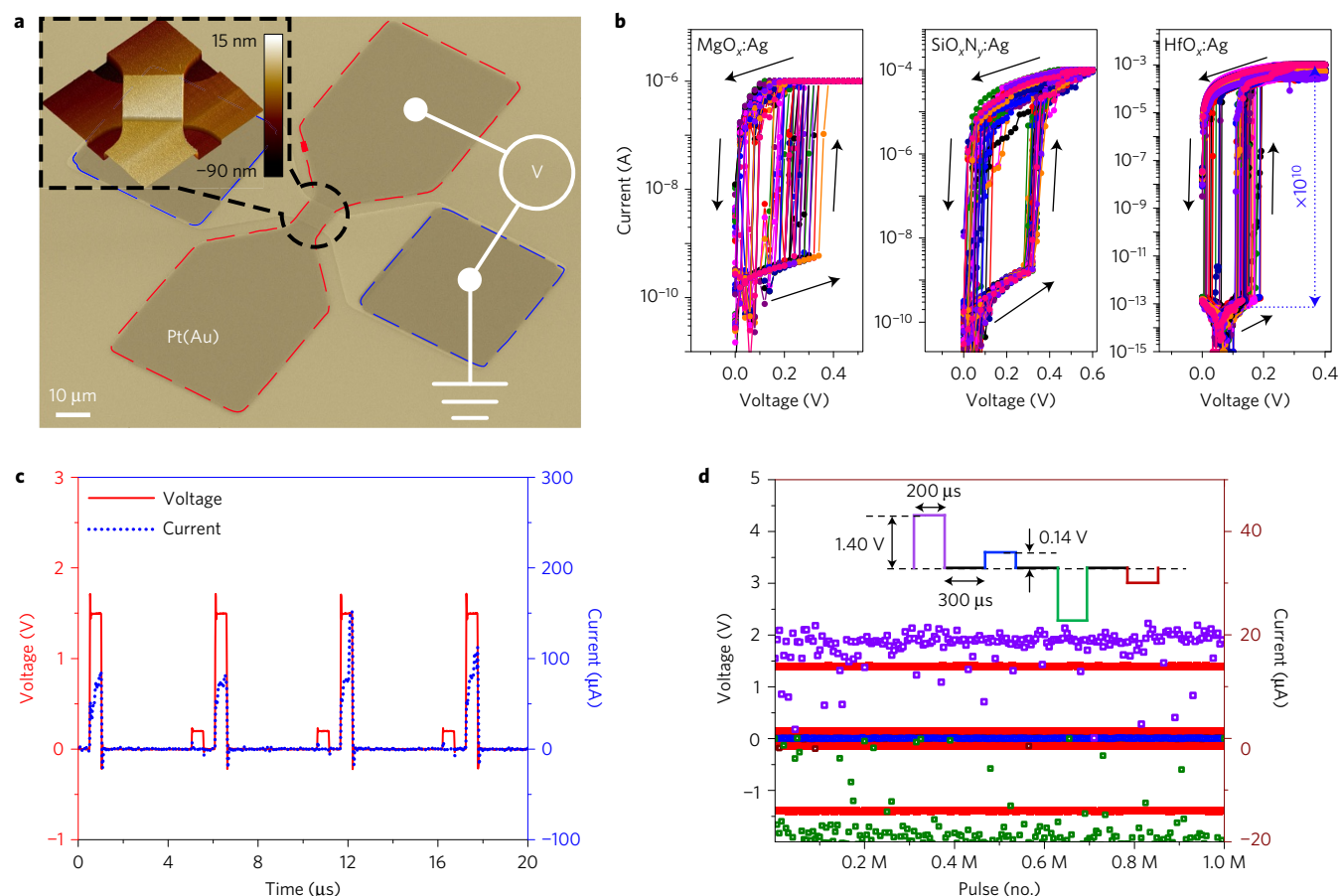


**Figure 1 | Highly nonlinear, fast and repeatable threshold switching behaviours of diffusive memristors.** **a**, Pseudo-colour scanning electron micrograph of a crossbar device. Top electrodes are depicted by the red dashed line and bottom contacts by the blue dashed lines. Biasing is applied on the top electrode with the bottom electrode grounded. The inset shows an atomic force micrograph of the junction. **b**, Repeatable highly nonlinear threshold switching  $I$ - $V$  loops for devices with different host lattices doped with silver. **c**, High-speed switching characteristics of the SiO<sub>x</sub>N<sub>y</sub>:Ag device at an elevated temperature of 600 K. The programming pulse width is 500 ns and the voltage is 1.5 V. **d**, Endurance-cycling performance test of the SiO<sub>x</sub>N<sub>y</sub>:Ag device for 1 million cycles at room temperature. The inset shows the shape of the applied voltage pulse, which consists of four segments: a 1.4 V/200 μs programming voltage and a 0.14 V/200 μs read voltage, followed by a -1.4 V/200 μs programming voltage and a -0.14 V/200 μs read voltage. We sampled one voltage and one current data point from each of the four segments of the pulse. The voltage samples are shown in red, while the purple dots and green dots correspond to device current due to positive and negative programming pulses, respectively. The read current for both positive and negative programming is at the instrument noise level (<100 nA) for the current measurement range used. The device did not fail during the measurement, demonstrating high robustness.

selectors for mitigating sneak current paths in crossbar arrays<sup>27–30</sup>. In Fig. 1c, each 500 ns/1.5 V switching pulse was followed by a 500 ns/0.2 V reading pulse to verify that the device had relaxed back to the insulating state under zero bias within 5 μs after switching to the high-conductance state. Repeatable and symmetric switching was demonstrated using wider bipolar voltage pulses with over a million switching cycles in Fig. 1d.

To examine the switching mechanism, especially the spontaneous relaxation to the insulating state on ceasing power, a planar Au/SiO<sub>x</sub>N<sub>y</sub>:Ag/Au device with a nano-junction was fabricated for *in situ* HRTEM characterizations (Supplementary Fig. 5a). Reliable threshold switching was observed under a 100 nA compliance in ambient conditions with a typical relaxation time constant of ~11 ms (Supplementary Fig. 5b,c). In the time sequence of HRTEM images in Fig. 2 (Supplementary Movies), the gap between the Au electrodes first experienced a constant voltage (20 V) with a 100 nA compliance from 0 s to 5 s, after which the power was turned off. We observed a delay time of ~2 s during which the measured current was <5 nA and Ag nanoparticles formed in the gap region (indicated by the orange and blue arrows at time 0.1 s), followed by an abrupt current jump to the compliance level as nanoparticles grew further to bridge the gap between the electrodes

(indicated by the red arrow at 2.5 s). At 4.6 s, the cluster reached a diameter of ~4.2 nm.

Up to this point, the behaviour of Ag nanoparticles in SiO<sub>x</sub>N<sub>y</sub> is similar to previous observations, which have been interpreted as electrochemical reactions at effectively bipolar electrodes<sup>21–26</sup>. We next turned off the power at 5.0 s to observe the spontaneous relaxation, which is critical for understanding the dynamics of these devices, but has not been previously reported to the best of our knowledge. The elongated cluster of nanoparticles that had probably formed the conductive bridge rapidly contracted from a length of 14.8 nm to a circular profile with a diameter of 7.6 nm by 5.7 s, indicating Ostwald ripening<sup>31</sup>. These observations demonstrated that minimizing the interfacial energy between the Ag nanoparticles and the dielectric served as the driving force for the relaxation dynamics of these diffusive memristors. The material systems exhibiting a substantial relaxation were those with large wetting contact angles<sup>32</sup>, such as MgO<sub>x</sub>:Ag, SiO<sub>x</sub>N<sub>y</sub>:Ag and HfO<sub>x</sub>:Ag in Fig. 1b, consistent with the reported pseudoelasticity of silver nanoparticles<sup>33</sup> and the hypothesis that interfacial energy facilitates filament rupture in volatile switching<sup>34–36</sup>.

The dynamical properties of diffusive memristors were further studied by applying voltage pulses and measuring resulting currents.



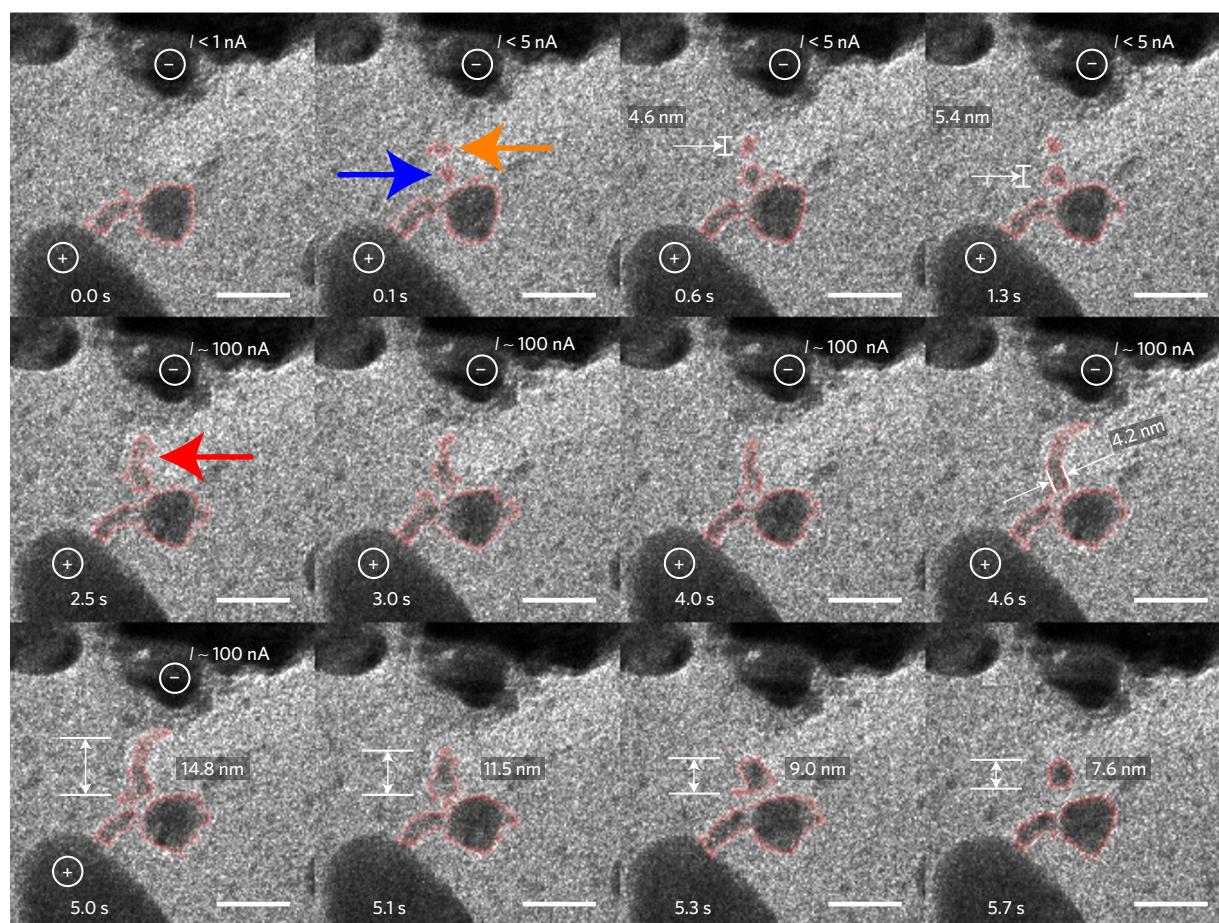


**Figure 2 | *In situ* TEM observation of the threshold switching process suggesting the relaxation is a diffusion process driven by interfacial energy minimization.** External electric field is exerted at the point of time zero. Ag migration is observed at time 0.1 s when two nanocrystals (orange and blue arrows) started to form. A clear arc-shaped filament is visible at 2.5 s (red arrow). When the external biasing is removed at 5.0 s, the filament starts to deform, shrinking to a round spherical nanocluster implying an interfacial energy driven diffusion mechanism. All scale bars, 20 nm.

Under an applied pulse, the device exhibited threshold switching to a low resistance state after an incubation period  $\tau_d$ , as shown in Fig. 3a. This  $\tau_d$  is related to the growth and clustering of silver nanoparticles to eventually form conduction channels. Following channel formation, the current jumped abruptly by several orders of magnitude, and then slowly increased further under bias as the channel thickened. As the voltage pulse ended, the device relaxed back to its original high-resistance state over a characteristic time  $\tau_r$ . As shown in Fig. 3b,  $\tau_r$  decreased as the ambient temperature increased, consistent with a diffusion activation energy of 0.27 eV (inset of Fig. 3b), and the characteristic time was on the same order as the response of bio-synapses, that is, tens of milliseconds. In addition to the temperature,  $\tau_d$  and  $\tau_r$  were also functions of the voltage pulse parameters, operation history, Ag concentration, host lattice, device geometry, humidity and other factors<sup>37–40</sup>, which alone or combined could be used to tune the desired dynamics for neuromorphic systems (Supplementary Fig. 6).

To better understand the switching mechanism, we performed simulations using a generalized model similar to the one utilized for non-volatile switching and current noise in TaO<sub>x</sub> memristors<sup>41</sup>. This model links electrical, nano-mechanical and thermal degrees of freedom (Methods). The model here did not include redox reactions, although they can be added to more closely resemble the electrochemical models proposed previously<sup>21–26</sup>.

In our simulations, two large clusters of metallic nanoparticles are located near each terminal of the device (Fig. 4a1). When a voltage pulse is applied (Fig. 4a), the local temperature increases

due to Joule heating and the potential is tilted by electric forces acting on particles with induced charge, both of which cause larger clusters to break up. As the nanoparticles become more uniformly distributed in the gap, the resistance drops, the current and temperature increase, and a positive feedback results in the formation of a conductive channel (Fig. 4a2). As soon as the power is turned off, the temperature drops, and the nanoparticles start to coalesce (Fig. 4a3), that is, particles slowly diffuse to their minimum energy positions near the device terminals. Eventually, most of the nanoparticles have merged into larger clusters to minimize interfacial energy, and the high-resistance state is re-established along with the original particle distribution almost restored (compare Fig. 4a1 and a4), leading to the observed volatility in Fig. 2. The model predicts interesting conductance evolution similar to synaptic behaviour when a train of pulses is applied (Fig. 4b). First, when the initial voltage pulse is applied, electric field-assisted diffusion pumps some of the Ag particles out of the 'left' cluster and they start to bridge terminals. However, a single short pulse cannot excite enough particles to form a complete conducting path between the two terminals (Fig. 4b2). If a subsequent pulse arrives before particles are reabsorbed, that is, if the time between pulses is shorter than the diffusion relaxation time, more particles are pushed into the gap between terminals resulting in a gradual increase in device conductance, similar to the paired-pulse facilitation (PPF) phenomenon in bio-synapses. The result is that when high-frequency pulses are applied, the device conductance increases with the number of pulses (Fig. 4b) until a conducting bridge is formed (Fig. 4b1–b4). Second, as the electric field

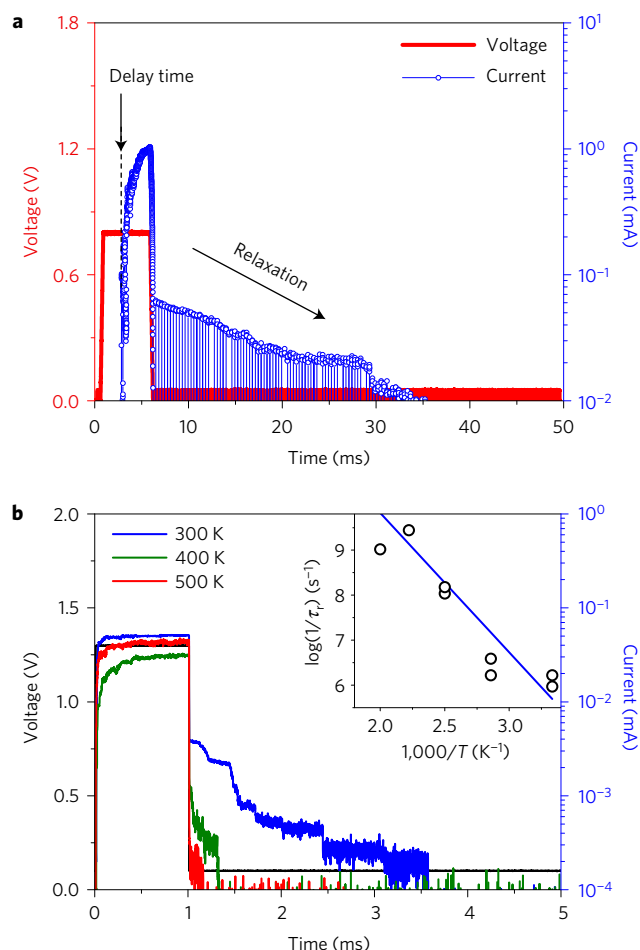


**Figure 3 | Timing characteristics of  $\text{SiO}_x\text{N}_y\text{:Ag}$  diffusive memristor.**

**a**, Delay and relaxation characteristics of the device showing variation of current (blue) with applied voltage (red) pulses. Multiple read voltage pulses (0.05 V, 10  $\mu\text{s}$ ) are used to study the device relaxation current after the switching pulse (0.75 V, 5 ms). The device requires a finite delay time to turn ON and has a finite relaxation time before it goes to the high-resistance state after the switching pulse is removed. **b**, Device relaxation performance showing the variation of current with applied voltage at different temperatures. The relaxation time decreases with increasing temperature. Inset shows the Arrhenius plot of the temperature dependence of the relaxation time. Each data point (black circles) is an average over 10 measured relaxation times, and these data points are fitted to the blue line. The activation energy for the material system is calculated to be 0.27 eV.

pumps more and more particles towards one of the device terminals, the number of particles at the other terminal decreases (Fig. 4b4,b5, where the distribution peak at the left terminal decreases as more and more pulses arrive). As a result, the number of particles in the gap decreases (Fig. 4b5,b6) and the device conductance starts to decay. This results in an inflection of the device conductance due to excessive stimulation, capturing another synaptic behaviour, that is, PPF followed by PPD (paired-pulse depression). Third, sequential high-voltage pulses with a long enough interval (low frequency) may form a conducting bridge first, but before the next pulse arrives the bridge breaks and the particles are reabsorbed at the terminals. Due to the electric field, the Ag particles gradually deplete at one terminal and accumulate at the other. Consequently, the conductance of the device starts to decrease from the initial state without showing facilitation first (PPD) (Supplementary Fig. 7c).

The simulations for Ag in dielectric agreed well with the experimental HRTEM observations. In addition, significant similarities

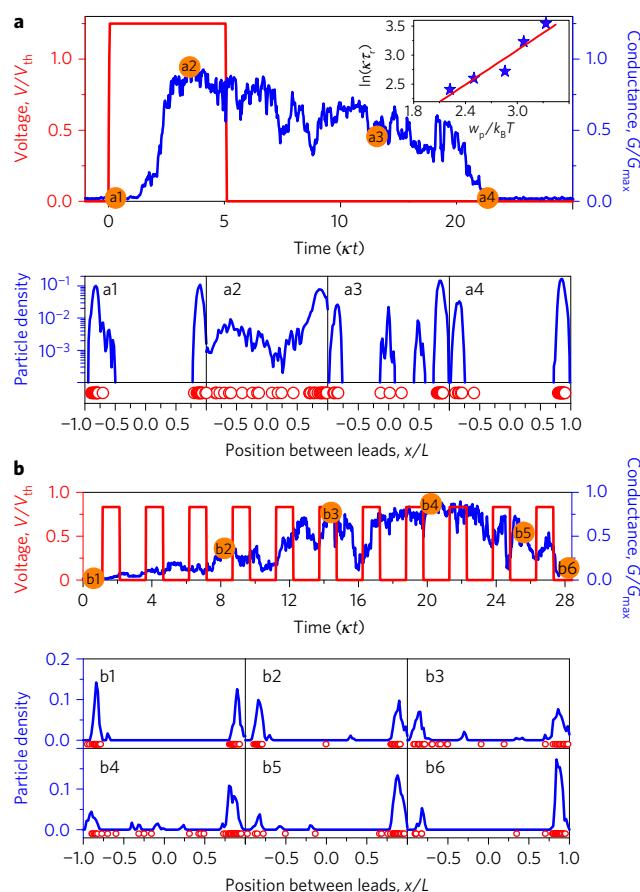


**Figure 4 | Simulated operation of a diffusive memristor device.**

**a**, The conductance response (blue curve) induced by a voltage pulse (red curve) shows a delay in the response and a gradual relaxation towards the low conducting state, consistent with the experimental threshold switching property in Fig. 3a. Panels a1–a4 show evolution of metallic nanoparticle density distributions. Blue curves represent particle distributions. Each curve was averaged over temporal interval  $0.2/\kappa$  around time moments indicated by orange dots (in **a**) when instantaneous particle snapshots (red dots) are plotted. The inset shows the temperature dependence of the relaxation time  $\tau$  defined as the time needed for the conductance to drop to value  $0.02G_{\text{max}}$  after switching the voltage, which agrees with that of Fig. 3b. The red curve is the fitting of  $\ln(\kappa\tau)$  by the function  $A + Bw_p/k_B T$  with  $A = 0.1$ ,  $B = 1$ . **b**, The simulated conductance response (blue curve) shows both facilitation and then depression following a sequence of short and frequent pulses (red curve). Panels b1–b6 show evolution of metallic nanoparticle density. Blue curves represent particle distributions; each curve was averaged over temporal interval  $0.02/\kappa$ , around time moments indicated by orange dots (in **b**) when instantaneous particle snapshots (red dots) are plotted. The conductance initially increases with number of pulses until a conducting bridge between terminals is formed. The conductance eventually saturates and drops as the number of pulses increases further, which captures an advanced synaptic behaviour, that is, PPF followed by PPD. Other simulation parameters are  $\lambda/2 = R_1 = 2R_p/3 = L/10$ ,  $x_c = 85L$ , we simulate 40 nano-metallic particles and the simulation step was  $dt = 2 \times 10^{-6}$  resulting in  $10^7$  steps during each simulation run; the reasoning of parameter choice and pinning parameters are discussed in the Methods.

exist between the Ag dynamics and that of synaptic  $\text{Ca}^{2+}$ , not only in the diffusion mechanism but also in their dynamical balance of concentration and regulating roles in their respective systems.  $\text{Ca}^{2+}$  dynamics is responsible for initiating both short- and long-term plasticity of synapses, forming the basis of memory and learning<sup>42–44</sup>.

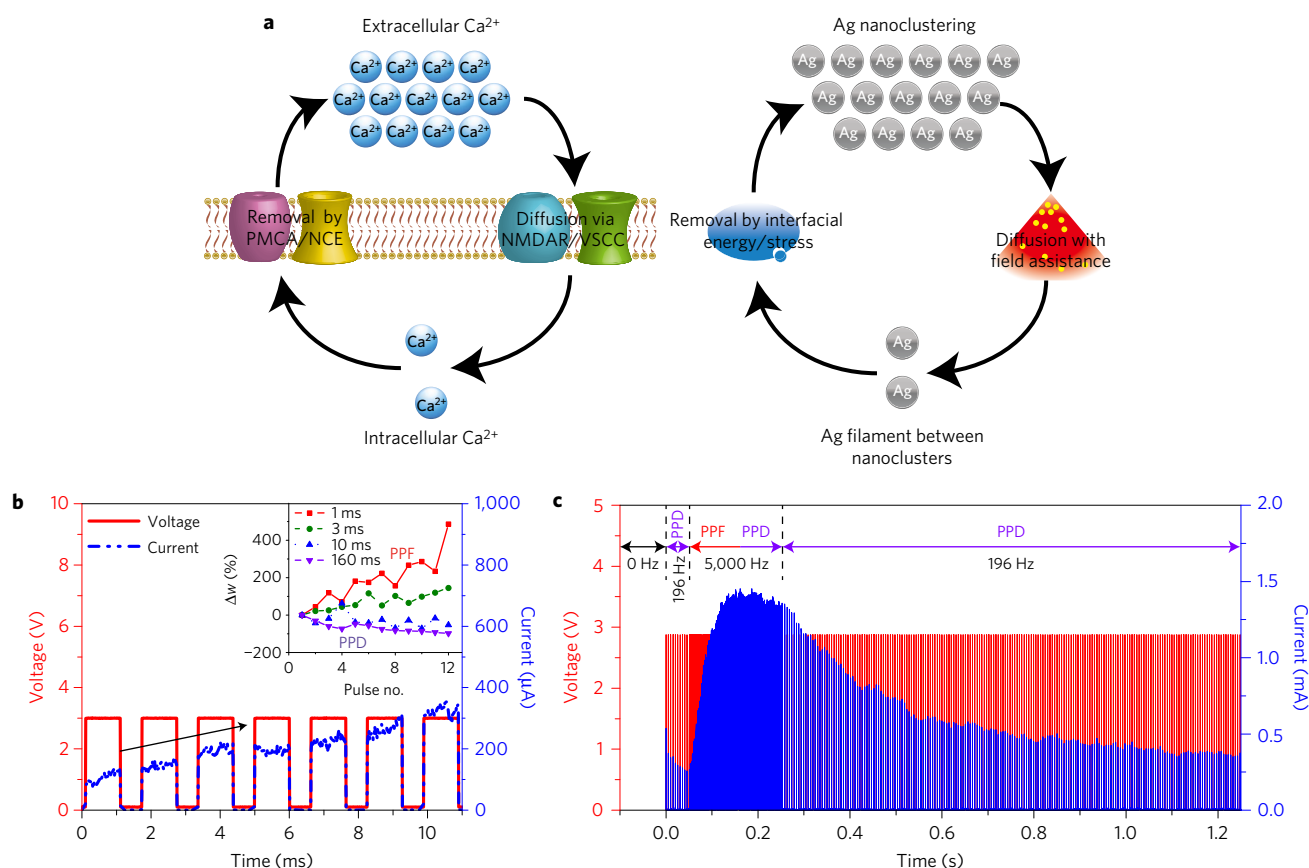


**Figure 5 | Schematic illustration of the analogy between  $\text{Ca}^{2+}$  and Ag dynamics, and short-term synaptic plasticity of the diffusive memristor.**

**a**, (left) Diffusion of  $\text{Ca}^{2+}$  from extracellular sources via voltage-sensitive calcium channels (VSCC) and *N*-methyl-D-aspartate receptors (NMDAR), and the removal of  $\text{Ca}^{2+}$  via the plasma membrane  $\text{Ca}^{2+}$ -ATPase (PMCA) and the  $\text{Na}^{+}/\text{Ca}^{2+}$  exchanger (NCE). (right) Ag diffusion into the gap region between Ag nanoclusters with field assistance and clearance of Ag filament from the gap region by the interfacial energy and possibly mechanical stress once the voltage signal is removed, which is a close emulation of  $\text{Ca}^{2+}$  dynamics. **b**, Experimental demonstration of short-term synaptic PPF and PPD behaviour with the diffusive  $\text{SiO}_x\text{N}_y\text{:Ag}$  memristor. Device current response (blue) to multiple subsequent voltage pulses (3 V, 1 ms). The duration between two pulses when the applied voltage is 0 V is denoted as  $t_{\text{zero}}$ . For small  $t_{\text{zero}}$ , the current increases with the number of pulses giving larger conductance (weight) change, demonstrating PPF. Inset shows the percentage change in conductance (weight) for different  $t_{\text{zero}}$  values. As the  $t_{\text{zero}}$  increases from 1 ms to 160 ms, the weight change slows down with increasing pulse number and eventually becomes negative. **c**, Experimental demonstration of PPD following PPF in the diffusive  $\text{SiO}_x\text{N}_y\text{:Ag}$  memristor. Device current (blue) response to a train of voltage pulses (2.8 V, 100 μs) of the same amplitude but different frequencies. The device begins with PPD (depression) following low-frequency (196 Hz) stimulation and experiences an increase in current (facilitation) once the stimulation frequency is raised (5,000 Hz). The brief facilitation is followed by depressed current under identical stimulation frequency (5,000 Hz) but excessive pulse number, as a result of the gradual depletion of silver at one electrode and accumulation at the other. The current relaxes to its initial value with subsequent low-frequency stimulation (196 Hz), implying potential for autonomic computing<sup>48,49</sup>.

In chemical synapses, the dynamical balance of the  $\text{Ca}^{2+}$  concentration is shaped by both influx via voltage-sensitive calcium channels and *N*-methyl-D-aspartate receptors<sup>42,43</sup>, and extrusion via the plasma membrane  $\text{Ca}^{2+}$ -ATPase and the  $\text{Na}^{+}/\text{Ca}^{2+}$  exchanger<sup>43,44</sup> that restores  $[\text{Ca}^{2+}]_i$  to the basal concentration. The  $\text{Ca}^{2+}$  dynamics naturally leads to short-term plasticity in which residual elevation of presynaptic  $[\text{Ca}^{2+}]_i$  directly correlates to the enhancement of synaptic transmission<sup>43–45</sup>. The calcium inside the postsynaptic membrane also plays important regulating roles in long-term potentiation and depression where  $\text{Ca}^{2+}$  accumulation is necessary to regulate enzymes, that is,  $\text{Ca}^{2+}$ /calmodulin-dependent protein kinase II (CaMKII), calcineurin and protein phosphatase 1 (refs 42, 43, 46, 47), which in turn triggers rapid and persistent modification of synaptic strengths by changing the number and/or conductance of  $\alpha$ -amino-3-hydroxy-5-methyl-4-isoxazolepropionic acid receptors<sup>43,46,47</sup>. The Ag diffusion into the gap region between Ag nanoclusters with field assistance (Figs 2 and 4), resembles the influx processes of  $\text{Ca}^{2+}$ . The clearance of bridging Ag nanoparticles from the gap region by interfacial energy and possibly mechanical stress

when electrical stimulus is removed replicates the extrusion processes of  $\text{Ca}^{2+}$ . Thus, the Ag dynamics of the diffusive memristor is a functional emulation of bio-synapses (Fig. 5a). An expected characteristic of diffusive memristors is short-term plasticity, where application of paired pulses to synapses can induce an increase or decrease in postsynaptic responses, depending on the frequency of applied pulses. As shown in Fig. 5b, when the time interval between pulses ( $t_{\text{zero}}$ ) is short (high frequency), the device conductance increases (PPF) from its initial conductance (steady state of the diffusive memristor) as the number of pulses increases. In contrast, a long  $t_{\text{zero}}$  (low frequency) leads to a reduced rate of increment or even a decrease in conductance (PPD) from the same initial conductance (inset of Fig. 5b and Supplementary Fig. 7a,b)<sup>45,48</sup>. Moreover, it has also been shown in bio-synapses that prolonged or excessive stimulations with high-frequency (short  $t_{\text{zero}}$ ) pulses will eventually lead to an inflection from facilitation to depression, an effect solely induced by an increased number of stimulation pulses at the same frequency<sup>45</sup>. This important feature of bio-synapses, which has not been clearly demonstrated previously on two-terminal devices, was



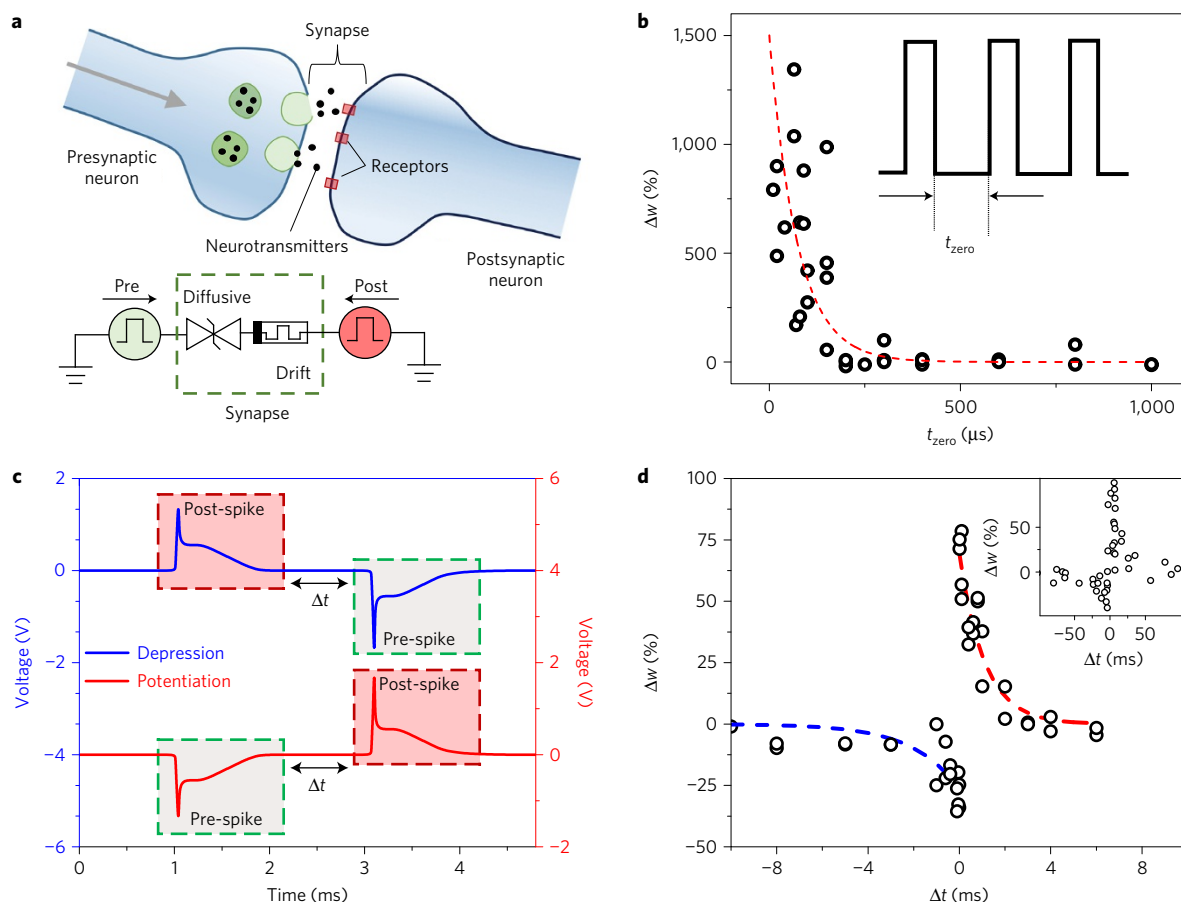


**Figure 6 | Bio-realistic long-term plasticity.** **a**, Illustration of a biological synaptic junction between the pre- and postsynaptic neurons. Also shown is the electrical implementation, a circuit diagram of the electronic synapse consisting of the  $\text{SiO}_x\text{N}_y\text{:Ag}$  diffusive memristor connected in series with the  $\text{TaO}_x$  drift memristor and between pulsed voltage sources, which act as neurons that send voltage spikes to the synaptic junction. **b**, SRDP showing the change in the conductance (weight) of the drift memristor in the electronic synapse with change in the duration  $t_{zero}$  between the applied pulses. For long  $t_{zero}$ , the change in the conductance of the diffusive memristor is lower (see Fig. 5b), resulting in a lower weight change of the drift memristor. As the  $t_{zero}$  decreases, the weight change increases. The dashed red line represents a fit of the average conductance change with change in  $t_{zero}$ . **c**, Schematic of the pulses applied to the combined device for STDP demonstration. The long low-voltage pulse in each spike turns the diffusive memristor ON, and the short high-voltage pulse switches the drift memristor. When the post-spike precedes the pre-spike, the device is reset (depressed), and when the pre-spike precedes the post-spike, the device is set (potentiated). The timing ( $\Delta t$ ) between the two spikes determines the voltage drop across the drift memristor. **d**, Plot of the conductance (weight) change of the drift memristor with variation in  $\Delta t$  showing the STDP response of the electronic synapse. This response is characteristic of the timing-dependent response of biological synapses. The inset shows the STDP of a typical chemical synapse (reprinted from Fig. 7 of ref. 50).

predicted in Fig. 4b and observed experimentally in Fig. 5c. The device in its steady state shows PPD following low-frequency (196 Hz) stimulation and experiences an increase in current (facilitation) once the stimulation frequency is raised (5,000 Hz). The facilitation turns into depression (current decrease) with more pulses having identical frequency (5,000 Hz) due to the gradual depletion of silver at one electrode and accumulation at the other. The depression continues with the low-frequency (196 Hz) pulses, which eventually bring the device back to a state close to its initial steady state, implying the potential for autonomic computing<sup>48,49</sup>.

The above PPF and PPD demonstrations were realized with diffusive memristors alone, resembling short-term plasticity<sup>45</sup> in synapses because any conductance change from the OFF state of diffusive memristors will vanish over time. When combined with a non-volatile element, that is, a drift-type memristor, long-term plasticity<sup>50</sup> following the spike-rate-dependent plasticity (SRDP) and STDP<sup>47,50</sup> learning rules can be realized. For demonstration purposes, we created a combined circuit element using a diffusive memristor in series with a  $\text{Pt/TaO}_x/\text{Ta/Pt}$  drift memristor (Supplementary Fig. 8). This combined element was connected to pulsed

voltage sources similar to a synapse between pre- and postsynaptic neurons (Fig. 6a). The SRDP demonstration is illustrated in Fig. 6b, where the drift memristor weight (conductance) change is a function of the frequency of the applied pulses. Similar to Fig. 5b, a shorter  $t_{zero}$  resulted in a greater increase in the conductance of the diffusive memristor and thus a larger voltage drop across the drift memristor, which thereby switched due to the voltage divider effect. A longer  $t_{zero}$  resulted in a smaller increase in the diffusive memristor conductance and thus a smaller voltage drop across the drift memristor, leading to a smaller or non-detectable resistance change in the drift memristor.

To demonstrate the STDP learning rule with non-overlapping spikes, pre- and postsynaptic spikes (Fig. 6c) were applied to the combined element. The two spikes were separated by a time difference  $\Delta t$ , which determined how much conductance change was programmed in the drift memristor. Each spike consisted of two parts, a high-voltage short pulse and a low-voltage long pulse. The pre-spike and post-spike were equal in magnitude but opposite in voltage polarity (Fig. 6c). In the combined element, the resistance of the diffusive memristor in its OFF state is much larger than that

of the drift memristor, while the resistance of its ON state is much smaller than that of the drift memristor. As the diffusive memristor has a finite delay time, the short high-voltage pulse will not turn it ON. In contrast, the long voltage pulse with a lower amplitude will turn ON the diffusive memristor. The drift memristor is not switched by the first spike, because the majority of the voltage drops across the diffusive memristor and turns it ON first. After the spike ends, the resistance of the diffusive memristor gradually increases from its ON state over time, regulated by the diffusive dynamics. The second spike occurs at a time  $\Delta t$  from the end of the first spike, and it may or may not switch the drift memristor depending on how much voltage drops on the drift memristor, which is determined by the conductance of the diffusive memristor at that moment, a function of  $\Delta t$ . A smaller  $\Delta t$  corresponds to a smaller diffusive memristor resistance and results in a greater resistance change in the drift memristor and vice versa (Fig. 6d). If the pre-spike appears before the post-spike, the drift memristor conductance increases (potentiation). If the pre-spike follows the post-spike, depression occurs (Supplementary Fig. 9). As the dynamics of the diffusive memristor provides an intrinsic timing mechanism for the combined element, the SRDP and STDP do not require complex pulse engineering or spike overlapping. This substantially reduces the complexity of both circuit and algorithm design and enables low-energy operations. In addition, depending on the application, any non-volatile memristor (low/high retention, analog/digital) can be used along with the diffusive memristor, allowing a significantly broader choice of materials rather than relying on the properties of the drift memristor when used alone. (See Supplementary Fig. 10 for STDP demonstration with a Pt/HfO<sub>x</sub>/TiN drift memristor.)

In conclusion, we have constructed and demonstrated a new class of memristors as synaptic emulators that function primarily on the basis of diffusion (rather than drift) dynamics. The microscopic nature of both the threshold switching and relaxation of the diffusive memristor is revealed for the first time by *in situ* HRTEM and explained by nanoparticle dynamics simulation. The Ag dynamics of the diffusive memristors functionally resemble the synaptic Ca<sup>2+</sup> behaviour in chemical synapses and lead to a direct and natural emulation of multiple synaptic functions for both short-term and long-term plasticity, such as PPF, PPD, PPD following PPF, SRDP and STDP. In addition to providing a synapse emulator, the diffusive memristor can also serve as a selector with a large transient nonlinearity that is critical for the operation of a large crossbar array as a neural network. The results here provide an encouraging pathway toward synaptic emulation using diffusive memristors for neuromorphic computing.

## Methods

Methods and any associated references are available in the [online version of the paper](#).

Received 29 March 2016; accepted 17 August 2016;  
published online 26 September 2016

## References

- Diorio, C., Hasler, P., Minch, B. A. & Mead, C. A. A single-transistor silicon synapse. *IEEE Trans. Electron Dev.* **43**, 1972–1980 (1996).
- Indiveri, G., Chicca, E. & Douglas, R. A VLSI array of low-power spiking neurons and bistable synapses with spike-timing dependent plasticity. *IEEE Trans. Neural Netw.* **17**, 211–221 (2006).
- Bartolozzi, C. & Indiveri, G. Synaptic dynamics in analog VLSI. *Neural Comput.* **19**, 2581–2603 (2007).
- Chua, L. Memristor-The missing circuit element. *IEEE Trans. Circuit Theory* **18**, 507–519 (1971).
- Terabe, K., Hasegawa, T., Nakayama, T. & Aono, M. Quantized conductance atomic switch. *Nature* **433**, 47–50 (2005).
- Waser, R. & Aono, M. Nanoionics-based resistive switching memories. *Nat. Mater.* **6**, 833–840 (2007).
- Kwon, D.-H. *et al.* Atomic structure of conducting nanofilaments in TiO<sub>2</sub> resistive switching memory. *Nat. Nanotech.* **5**, 148–153 (2010).
- Wedig, A. *et al.* Nanoscale cation motion in TaO<sub>x</sub>, HfO<sub>x</sub> and TiO<sub>x</sub> memristive systems. *Nat. Nanotech.* **11**, 67–74 (2016).
- Jo, S. H. *et al.* Nanoscale memristor device as synapse in neuromorphic systems. *Nano Lett.* **10**, 1297–1301 (2010).
- Yu, S., Wu, Y., Jeyasingh, R., Kuzum, D. & Wong, H. S. P. An electronic synapse device based on metal oxide resistive switching memory for neuromorphic computation. *IEEE Trans. Electron Devices* **58**, 2729–2737 (2011).
- Ohno, T. *et al.* Short-term plasticity and long-term potentiation mimicked in single inorganic synapses. *Nat. Mater.* **10**, 591–595 (2011).
- Wang, Z. Q. *et al.* Synaptic learning and memory functions achieved using oxygen ion migration/diffusion in an amorphous InGaZnO memristor. *Adv. Funct. Mater.* **22**, 2759–2765 (2012).
- Lim, H., Kim, I., Kim, J. S., Hwang, C. S. & Jeong, D. S. Short-term memory of TiO<sub>2</sub>-based electrochemical capacitors: empirical analysis with adoption of a sliding threshold. *Nanotechnology* **24**, 384005 (2013).
- La Barbera, S., Vuillaume, D. & Alibart, F. Filamentary switching: synaptic plasticity through device volatility. *ACS Nano* **9**, 941–949 (2015).
- Prezioso, M. *et al.* Training and operation of an integrated neuromorphic network based on metal-oxide memristors. *Nature* **521**, 61–64 (2015).
- Pershin, Y. V. & Di Ventra, M. Experimental demonstration of associative memory with memristive neural networks. *Neural Netw.* **23**, 881–886 (2010).
- Pershin, Y. V. & Di Ventra, M. Practical approach to programmable analog circuits with memristors. *IEEE Trans. Circuits Syst. I* **57**, 1857–1864 (2010).
- Pershin, Y. V. & Di Ventra, M. Memristive circuits simulate memcapacitors and meminductors. *Electron. Lett.* **46**, 517–518 (2010).
- Kim, S. *et al.* Experimental demonstration of a second-order memristor and its ability to biorealistically implement synaptic plasticity. *Nano Lett.* **15**, 2203–2211 (2015).
- Du, C., Ma, W., Chang, T., Sheridan, P. & Lu, W. D. Biorealistic implementation of synaptic functions with oxide memristors through internal ionic dynamics. *Adv. Funct. Mater.* **25**, 4290–4299 (2015).
- Xu, Z., Bando, Y., Wang, W., Bai, X. & Goldberg, D. Real-time *in situ* HRTEM-resolved resistance switching of Ag<sub>2</sub>S nanoscale ionic conductor. *ACS Nano* **4**, 2515–2522 (2010).
- Liu, Q. *et al.* Real-time observation on dynamic growth/dissolution of conductive filaments in oxide-electrolyte-based ReRAM. *Adv. Mater.* **24**, 1844–1849 (2012).
- Yang, Y. *et al.* Observation of conducting filament growth in nanoscale resistive memories. *Nat. Commun.* **3**, 732 (2012).
- Yang, Y. *et al.* Electrochemical dynamics of nanoscale metallic inclusions in dielectrics. *Nat. Commun.* **5**, 4232 (2014).
- Tian, X. *et al.* Bipolar electrochemical mechanism for mass transfer in nanoionic resistive memories. *Adv. Mater.* **26**, 3649–3654 (2014).
- Hubbard, W. A. *et al.* Nanofilament formation and regeneration during Cu/Al<sub>2</sub>O<sub>3</sub> resistive memory switching. *Nano Lett.* **15**, 3983–3987 (2015).
- Jo, S. H., Kumar, T., Narayanan, S., Lu, W. D. & Nazarian, H. *Electron Devices Meeting (IEDM)* 6.7.1–6.7.4 (IEEE International, 2014).
- Song, J., Woo, J., Prakash, A., Lee, D. & Hwang, H. Threshold selector with high selectivity and steep slope for cross-point memory array. *IEEE Electron Device Lett.* **36**, 681–683 (2015).
- Yang, H. *et al.* 2015 Symp. VLSI Technology (VLSI Technology) T130–T131 (IEEE International, 2015).
- Luo, Q. *et al.* *Electron Devices Meeting (IEDM)* 10.14.11–10.14.14 (IEEE International, 2015).
- Voorhees, P. W. The theory of Ostwald ripening. *J. Stat. Phys.* **38**, 231–252 (1985).
- Stoneham, A. M. Systematics of metal–insulator interfacial energies: a new rule for wetting and strong catalyst-support interactions. *Appl. Surf. Sci.* **14**, 249–259 (1983).
- Sun, J. *et al.* Liquid-like pseudoelasticity of sub-10-nm crystalline silver particles. *Nat. Mater.* **13**, 1007–1012 (2014).
- Valov, I. & Staikov, G. Nucleation and growth phenomena in nanosized electrochemical systems for resistive switching memories. *J. Solid State Electrochem.* **17**, 365–371 (2012).
- van den Hurk, J., Linn, E., Zhang, H., Waser, R. & Valov, I. Volatile resistance states in electrochemical metallization cells enabling non-destructive readout of complementary resistive switches. *Nanotechnology* **25**, 425202 (2014).
- Guzman, D. M., Onofrio, N. & Strachan, A. Stability and migration of small copper clusters in amorphous dielectrics. *J. Appl. Phys.* **117**, 195702 (2015).
- Hasegawa, T., Terabe, K., Tsuruoka, T. & Aono, M. Atomic switch: atom/ion movement controlled devices for beyond von-Neumann computers. *Adv. Mater.* **24**, 252–267 (2012).
- Valov, I. *et al.* Atomically controlled electrochemical nucleation at superionic solid electrolyte surfaces. *Nat. Mater.* **11**, 530–535 (2012).

39. Tsuruoka, T. *et al.* Effects of moisture on the switching characteristics of oxide-based, gapless-type atomic switches. *Adv. Funct. Mater.* **22**, 70–77 (2012).
40. Valov, I. & Lu, W. D. Nanoscale electrochemistry using dielectric thin films as solid electrolytes. *Nanoscale* **8**, 13828–13837 (2016).
41. Yi, W. *et al.* Quantized conductance coincides with state instability and excess noise in tantalum oxide memristors. *Nat. Commun.* **7**, 11142 (2016).
42. Burgoyne, R. D. Neuronal calcium sensor proteins: generating diversity in neuronal  $\text{Ca}^{2+}$  signalling. *Nat. Rev. Neurosci.* **8**, 182–193 (2007).
43. Clapham, D. E. Calcium signaling. *Cell* **131**, 1047–1058 (2007).
44. Catterall, W. A. & Few, A. P. Calcium channel regulation and presynaptic plasticity. *Neuron* **59**, 882–901 (2008).
45. Zucker, R. S. & Regehr, W. G. Short-term synaptic plasticity. *Annu. Rev. Physiol.* **64**, 355–405 (2002).
46. Malenka, R. C. & Bear, M. F. LTP and LTD: an embarrassment of riches. *Neuron* **44**, 5–21 (2004).
47. Caporale, N. & Dan, Y. Spike timing-dependent plasticity: a Hebbian learning rule. *Annu. Rev. Neurosci.* **31**, 25–46 (2008).
48. Feng, L., Molnár, P. & Nadler, J. V. Short-term frequency-dependent plasticity at recurrent mossy fiber synapses of the epileptic brain. *J. Neurosci.* **23**, 5381–5390 (2003).
49. Mulkey, R., Herron, C. & Malenka, R. An essential role for protein phosphatases in hippocampal long-term depression. *Science* **261**, 1051–1055 (1993).
50. Bi, G.-q. & Poo, M.-m. Synaptic modifications in cultured hippocampal neurons: dependence on spike timing, synaptic strength, and postsynaptic cell type. *J. Neurosci.* **18**, 10464–10472 (1998).

## Acknowledgements

This work was supported in part by the US Air Force Research Laboratory (AFRL) (Grant No. FA8750-15-2-0044), the Intelligence Advanced Research Projects Activity (IARPA) (contract 2014-14080800008), US Air Force Office for Scientific Research (AFOSR) (Grant No. FA9550-12-1-0038), and the National Science Foundation (NSF) (ECCS-1253073). Any opinions, findings and conclusions or recommendations expressed in this material are those of the authors and do not necessarily reflect the views of AFRL. Part of the device fabrication was conducted in the clean room of the Center for Hierarchical Manufacturing (CHM), an NSF Nanoscale Science and Engineering Center (NSEC) located at the University of Massachusetts Amherst. The TEM work used resources of the Center for Functional Nanomaterials, which is a US DOE Office of Science Facility, at Brookhaven National Laboratory under Contract No. DE-SC0012704. The authors thank M. McLean for useful discussions on computing.

## Author contributions

J.J.Y. conceived the concept. J.J.Y., Q.X., Z.W. and S.J. designed the experiments. Z.W. fabricated the devices and S.J. performed electrical measurements. S.E.S. performed the simulation. H.L.X. carried out the *in situ* TEM characterizations. H.J., R.M., P.L., M.H., N.G., J.P.S., Z.L., Q.W., M.B., G.-L.L. and R.S.W. helped with experiments and data analysis. J.J.Y., Q.X., Z.W., S.J., S.E.S. and R.S.W. wrote the paper. All authors discussed the results and implications and commented on the manuscript at all stages.

## Additional information

Supplementary information is available in the [online version of the paper](#). Reprints and permissions information is available online at [www.nature.com/reprints](http://www.nature.com/reprints). Correspondence and requests for materials should be addressed to J.J.Y.

## Competing financial interests

The authors declare no competing financial interests.



## Methods

**Preparation of crossbar samples.** The diffusive memristor devices were grown on p-type (100) Si wafer with 100 nm thermal oxide. The bottom electrodes were patterned by photolithography followed by evaporation and liftoff of a ~20-nm-thick Pt(Au) (99.99%, Kurt J. Lesker) layer. The ~15-nm-thick doped dielectric was deposited at room temperature by reactively co-sputtering MgO or HfO<sub>2</sub> (99.95%, Kurt J. Lesker) and Ag (99.99%, Kurt J. Lesker) in an ambient of mixed Ar and O<sub>2</sub>, or co-sputtering Si (99.99%, Kurt J. Lesker) and Ag in Ar, N<sub>2</sub> and O<sub>2</sub>. The ~30 nm Pt(Au) top electrodes were subsequently patterned by photolithography followed by evaporation and liftoff processes. Electrical contact pads of the bottom electrodes were first patterned by photolithography and then subjected to reactive ion etching with mixed CHF<sub>3</sub> and O<sub>2</sub> gases. The drift memristor devices used the same substrates and bottom electrodes as the diffusive memristor devices. The switching layer was grown by sputtering Ta<sub>2</sub>O<sub>5</sub> (HfO<sub>2</sub>) (99.99%, Kurt J. Lesker) for a thickness of ~10(5) nm in Ar gas followed by photolithography. Top electrodes were deposited by evaporating Ta(5 nm, 99.95%, Kurt J. Lesker)/Pt(20 nm) (sputtering TiN(50 nm, 99.5%, Kurt J. Lesker)/Pd(30 nm, 99.95%, Kurt J. Lesker)) and liftoff.

**Electrical measurements.** Electrical measurements were performed with the Keysight B1500A semiconductor device analyser using two of its modules: d.c. measurements were carried out using the source and measure units (B1517A) and the B1530A waveform generator/fast measurement unit (WGFMU) was used to perform the pulse measurements. Using a two-probe (W tips) configuration, we applied d.c. and pulse voltages between the top and bottom electrodes of the device and measured current through one of the measurement units. The same units were used to perform measurements at different temperatures on the Variable Temperature Micro Probe System (MMR Technologies, K2000 Digital Temperature Controller) in ambient atmosphere. We performed the SRDP and the STDP experiments with the diffusive memristor in series with a Pt/TaO<sub>2</sub>/Ta/Pt drift memristor. The B1530A WGFMU was used for applying the pre- and spike-postsynaptic voltage spikes. The conductance of the drift memristor was read using a small d.c. voltage between each programming operation to determine the change in its weight. For each data point of the SRDP measurement, the drift memristor was first initialized to its high-resistance state, and then we applied 15 voltage pulses across the combined series memristors with the same pulse amplitude (2.5 V), duration (40 μs) and a particular  $t_{\text{zero}}$  value, and finally read the drift memristor to determine the change in its state induced by the train of 15 pulses.

**Preparation of planar samples for TEM.** The specimen for *in situ* HRTEM was grown on the Aduro E-chip with pre-built Au connections (Model E-AEL00-LN, Protochip). Au electrodes are patterned by electron beam lithography followed by evaporation and liftoff of a ~20-nm-thick Au layer. The doped dielectric layer of SiO<sub>x</sub>N<sub>y</sub>:Ag was deposited by reactively co-sputtering of both Si and Ag targets in an ambient of Ar, N<sub>2</sub> and O<sub>2</sub> at room temperature with a thickness of ~30 nm.

***In situ* TEM.** The *in situ* HRTEM was performed at Brookhaven National Laboratory with the FEI Titan 80-300 operating at 300 keV. The sample was grown on an Aduro E-chip (Model E-AEL00-LN, Protochip) that was mounted on a corresponding Aduro TEM holder for FEI (Protochip). Current was monitored in real time on a Keithley 2602B System SourceMeter that exerted electrical bias.

**Diffusive memristor dynamical simulations.** The diffusive memristor model links electrical, nano-mechanical and heat degrees of freedom: the growth, shape change and decay of clusters of nanoparticles identified by their positions  $x_i$  inside a device ( $i$  is the nanoparticle label); the electric current through the device governed by a sequence of tunnelling resistances between nanoparticles; and the local temperature controlling the nanoparticle diffusion, determined by Joule heating and the thermal conductivity of the memristor.

The mathematical definition for a generic memristor<sup>4</sup> has two components, the quasi-static conduction equation relating voltage  $v$  and current  $i$ , or Ohm's law for the element

$$v = iR(x) \quad (1)$$

where  $R$  is the state-dependent resistance and  $x$  represents one or more state variables that define the physical properties of the memristor, and the dynamical equation(s) that define the evolution of the state variables with time in the presence of a current and affected by local temperature  $T$ :

$$\frac{dx}{dt} = f(x; i, T) \quad (2)$$

For the state-dependent resistance we assume sequential electron tunnelling: first from the input terminal to the nearest metallic nanoparticle, and then from this nanoparticle to the next one and so on with the last tunnelling event to the output

terminal. The total resistance of the memristor is the sum of tunnelling resistances between  $N-1$  adjacent nanoparticles/islands:

$$R_M = \sum_{i=0}^{N-1} R_i \exp[(x_{i+1} - x_i)/\lambda] \quad (3)$$

where  $\lambda$  is the effective tunnelling length,  $R_i$  is the tunnelling resistance amplitude (assumed the same for all islands), and  $x_0$  and  $x_N$  are the spatial coordinates of the input and output terminals, respectively, and we order the island positions as  $x_0 < x_1 < x_2 < \dots < x_{N-1} < x_N$ . The minimum resistance can be estimated as  $R_{\min} = \min R_M = NR_i \exp[2L/N\lambda]$ .  $L$  is the half size of the device.

To describe the nanoparticle diffusion, and thus the memristor dynamics, we employed an over-damped Langevin equation for each mobile metallic nanoparticle trapped by a potential  $U$  and subject to a random force  $\xi_i$ , the magnitude of which is determined by the device local temperature  $T$ ,

$$\eta \frac{dx_i}{dt} = -\frac{\partial U(x_i)}{\partial x_i} + \alpha \frac{V(t)}{L} + \sqrt{2\eta k_B T} \xi_i \quad (4)$$

In equation (4), the friction term (left-hand side), proportional to the particle velocity and viscosity  $\eta$ , is balanced by all other forces acting on nanoparticles. The first term on the right-hand side of equation (4) forces the nanoparticle to approach the minimum potential energy with a speed that is proportional to minus the local gradient of the potential energy. The drift term  $\alpha V(t)/L$  represents a bias in the electric field  $E = V(t)/L$  affecting nanoparticles with induced charge  $\alpha$  when the voltage,  $V(t)$ , is on. The electrical bias together with diffusion is responsible for switching to a high conducting state and depletion of nanoparticles at one of the device terminals. The random force,  $\sqrt{2\eta k_B T} \xi_i$ , which is driven by the instantaneous temperature, describes diffusion of the nanoparticles that occurs both when voltage is on and when the system relaxes with no bias toward the potential minimum after the power to the device is off and the local temperature cools. In other words, since  $T$  is nonzero, there will always be some diffusion of the nanoparticles modelled by adding random thermal fluctuations  $\xi_i$ , which are  $\delta$ -correlated white noise characterized by  $\langle \xi \rangle = 0$  and  $\langle \xi(0)\xi(t) \rangle = \delta(t)$ .

The potential  $U = U_i + U_p$  has two energy scales—the interfacial energy  $U_i$  responsible for formation of large metallic clusters near the device terminals and a weaker nanoparticle-pinning energy  $U_p$  with many smaller wells between the electrodes. Pinning can occur through interactions of the nanoparticles with impurities, the substrate and/or the ionic lattice<sup>41</sup>. For our simulations, we used  $U_i = -w_i [\exp(-(x_i + x_c)^2/R_i^2) + \exp(-(x_i - x_c)^2/R_i^2)]$  and  $U_p = (w_p/2) \sin(2\pi(x/R_p))$ , with the interfacial energy barrier  $w_i$  and the amplitude  $w_p$  of the pinning potential;  $x_c$  and  $-x_c$  are locations of large clusters formed due to interfacial energy. The particular shape of neither the interfacial potential nor the pinning energy profile is essential; the only property that matters is that the potential  $U$  has two different energy scales and the weaker pinning potential has many wells (for example, it can be random with fluctuating  $w_p$  and  $R_p$ ). At high enough temperature during a voltage pulse, the increased diffusion assisted by the electrical force breaks up the large nanoparticle clusters and populates the pinning sites. At lower temperatures after the power is off and the potential bias disappears, the nanoparticles re-aggregate to form clusters at the electrodes. Moreover, a qualitatively similar result (although requiring considerably more computational resources) has been obtained when we modelled the interfacial energy as an interaction between particles<sup>41</sup>.

The temperature dynamics are determined by Newton's law of cooling:

$$\frac{dT}{dt} = C_T Q - \kappa (T - T_0) \quad (5)$$

with the Joule heating power  $Q = V^2/R_M$  increasing the temperature of the system and thermal conductivity acting as a damping factor by removing energy from the system. Here,  $\kappa$  and  $C_T$  are the heat transfer coefficient and heat capacitance respectively, while the background temperature is  $T_0$ . Equations (4) and (5) are sufficient to describe the memristor dynamics subject to the current through the device, which is controlled by the electric circuit in which it is embedded. Thus, the model described above enables the simulation of a complex system consisting of both volatile and non-volatile memristors.

There are two timescales in the model, the diffusion timescale and the characteristic scale of temperature relaxation. The first one depends on temperature, potential profile, and electric drift; thus, this timescale changes depending on voltage pulse intensity and temperature. For this reason, we measure time in the simulations in units of the temperature relaxation time  $1/\kappa$ . As one can see from Fig. 4, the relaxation occurs on timescales of the order  $10-20\ 1/\kappa$ ; thus, the simulated system is clearly governed by diffusion rather than the temperature relaxation<sup>19</sup>. There are two conductance states with low and high conductance. We used the conductance  $1/R_{\min}$  in the high-conductance state as a normalization factor. The normalization enabled the simulated conductance to be plotted

as a percentage of its maximum conductance after each applied pulse, for instance, from Fig. 4b we conclude that the conductance reached 25% of the maximum after 4 pulses and about 75% after 7 pulses. To provide a better link to the experimental data, we normalized the voltages to the threshold voltage  $V_{th}$ , which was assumed to be the voltage where the conductance reached 10% of its maximum value. These quantities can be easily obtained from both simulations (averaged over 30 realizations) and experimental I–V hysteresis loops, thus directly linking the units in the simulations and the experiments. For the sake of consistency, we normalized all voltages to  $V_{th}$  at the highest simulated temperature,  $(k_B T/w_p) = 0.45$ . The temperature  $(k_B T/w_p)$  in the simulations was varied from 0.3 to 0.45 (that is, the same relative range as in Fig. 3b). In this range, the characteristic single-hopping timescale  $e^{w_p/k_B T}$  changed from about  $2/\kappa$  to  $6/\kappa$  and the diffusion relaxation time (estimated as a characteristic jump time multiplied by the number of jumps to reach

the interfacial minimum near the device terminal) was about  $20/\kappa$  to  $60/\kappa$ . The ratio of interfacial and pinning potentials  $w_i/w_p$  was assumed to be 4.5 in the simulations to ensure that the interfacial potential was strong enough to re-trap the Ag nanoparticles after the voltage was switched off and the thermal fluctuations were too weak to destroy the large clusters near the terminals in the absence of excess heating. Conversely, the electric force ( $\alpha V_{th} R_p/w_i = 0.3$  in the simulations) was used to suppress the interfacial barrier  $k_B w_i/T_0$  to about 3.6, which enabled the enhanced thermal fluctuations induced by Joule heating to activate the positive thermal feedback. The stronger fluctuations support larger Joule heating and vice versa, breaking up the large Ag clusters to form a string of smaller nanoparticles and thus a conductive path between the terminals, as observed experimentally in the HRTEM studies. Note that we also linked some model parameters with experimentally measurable ones, for example,  $C_T \approx \kappa w_p R_i/V_{th}^2 k_B$ ,  $\eta \approx w_p/\kappa L^2$  and  $\alpha \approx \eta \kappa L^2/V_{th}$ .